Magnetospheric Multiscale observations of Earth's oblique bow shock reformation by foreshock ultra-low frequency waves

Terry Z. Liu[1,2], Yufei Hao[3], Lynn B. Wilson III[4], Drew L. Turner[5], and Hui Zhang[2]

[1]Cooperative Programs for the Advancement of Earth System Science, University Corporation for Atmospheric Research, Boulder, CO, USA. [2]Geophysical Institute, University of Alaska, Fairbanks, Fairbanks, AK, USA. [3]Key Laboratory of Planetary Sciences, Purple Mountain Observatory, Chinese Academy of Sciences, Nanjing, China. [4]NASA Goddard Space Flight Center, Heliophysics Science Division, USA. [5]Johns Hopkins University Applied Physics Laboratory, Laurel, Maryland, USA.

Key Points

1. MMS in a string-of-pearls formation observed oblique bow shock reformation induced by foreshock ULF waves.

2. We propose the reformation mechanism is the periodic modification of the bow shock upstream conditions by the ULF waves.

3. The bow shock reformation generated ULF perturbations in the magnetosheath and modulated reflected ions.

Abstract

Collisionless shocks can be nonstationary with periodic reformation shown in many simulation results, but direct observations are still tenuous and difficult to conclusively interpret. In this study, using Magnetospheric Multiscale (MMS) observations, we report direct observational evidence of Earth's oblique bow shock reformation driven by the foreshock ultra-low frequency (ULF) waves.

When the four MMS spacecraft were in a string-of-pearls formation roughly along the bow shock normal, they observed that when each period of foreshock ULF waves encountered the bow shock, a new shock ramp formed. Meanwhile, in the magnetosheath, the old bow shock's remnants were observed periodically convecting downstream. We propose that the reformation mechanism of the oblique bow shock is the variation of the upstream conditions by the periodic ULF waves as they encounter the bow shock. We also examine the nature of reflected ions during the reformation process.

1. Introduction

Collisionless shocks are a fundamental and prevalent phenomenon in various plasma environments, playing an important role in particle acceleration (see review by Treumann (2009) and references therein). Based on the angle between the upstream magnetic field and the shock normal unit vector, θ_{Bn}, shocks can be categorized as quasi-parallel shocks ($\theta_{Bn} < \sim 45°$) and quasi-perpendicular shocks ($\theta_{Bn} > \sim 45°$). At quasi-parallel shocks, a portion of the solar wind particles are reflected back into the upstream region forming the foreshock (e.g., Eastwood et al., 2005) and driving the growth of ultra-low frequency (ULF) waves (e.g., Wilson, 2016). For example, there are "30 second waves" (e.g., Fairfield, 1969), which are intrinsically right-hand polarized magnetosonic modes (Hoppe and Russell, 1983; Eastwood et al., 2002), magnetosonic-whistler "1 Hz waves" (e.g., Fairfield, 1974), and short large-amplitude magnetic structures (SLAMS) (e.g., Schwartz et al., 1992).

Collisionless shocks can be nonstationary. For example, there are surface waves at shock fronts leading to rippled shock surfaces at ion-kinetic scales (e.g., Johlander et al., 2016; Gingell et al., 2017), which can affect the electron acceleration process (Umeda et al., 2009). There are also fluid-scale ripples which can affect the dynamics of reflected ions (Hao et al., 2016) and result in magnetosheath jets (e.g., Hietala et al., 2009; Hietala and Plaschke, 2013) that can cause perturbations in the magnetosphere-ionosphere system (e.g., Archer et al., 2013; Hietala et al., 2012; Wang et al., 2018) and accelerate particles (Liu et al., 2019, 2020a, 2020b).

Additionally, Burgess (1989) found from 1-D hybrid simulations that the transition region of quasi-parallel shocks can reform and periodically change from steepened to extended (in the direction along the shock normal) due to upstream perturbations. These results were later confirmed by 2-D simulations showing the reformation was not caused by the 1-D limitation (Thomas et al., 1990). In 3-D hybrid simulations, shock reformation was also seen (e.g., Lin and Wang, 2005). As shock reformation does not occur in MHD simulations, the ion kinetic process should play an important role. Multiple reformation mechanisms have been identified from simulations. For example, at nearly perpendicular shocks ($\theta_{Bn} > 80°$), the accumulation of specularly reflected ions at the upstream edge of the foot can increase the plasma density and magnetic field leading to a new shock front (e.g., Matsukiyo and Scholer, 2006; Scholer and Burgess, 2007). At quasi-parallel shocks, on the other hand, the reflected ions can interact with upstream ULF waves causing them to steepen to pulsation-like structures (Scholer, 1993) which ultimately become the reformed shock (Scholer and Burgess, 1992; Scholer et al., 1993). This reformation process has also been confirmed by recent simulations (e.g., Su et al., 2012a, 2012b; Hao et al., 2017). There are also other reformation mechanisms, such as interface instability (Winske et al., 1990) and whistler wave steepening (e.g., Scholer and Burgess, 2007). Additionally, in global hybrid simulations (Omidi et al., 2010, 2020; Liu et al., 2018), the secondary shock of foreshock bubbles (Turner et al., 2013, 2020; Liu et al., 2015, 2016) convects anti-sunward and becomes the Earth's new bow shock on a global scale.

Although many shock reformation processes have been simulated, direct observations are still limited (e.g., Lobzin et al., 2007; Lefebvre et al., 2009; Dimmock et al., 2019; Madanian et al., 2020; Yang et al., 2020). In early 2019, Magnetospheric Multiscale (MMS) spacecraft were in a string-of-pearls formation with separation of 100s of km, which provides a good opportunity to observe the evolution of the bow shock. In this study using MMS data, we present the direct observational evidence of the bow shock reformation caused by the upstream ULF waves.

2. Data

We used data from NASA's Magnetospheric Multiscale mission (MMS; Burch et al., 2016). We analyzed plasma data from the Fast Plasma Investigation instrument (Pollock et al., 2016), DC magnetic field data from the fluxgate magnetometer (Russell et al., 2016), and electric field data from axial and spin-plane double-probe electric-field sensors (Ergun et al., 2016; Lindqvist et al., 2016). From February to March 2019, the MMS spacecraft were in a string-of-pearls formation with separation of several hundred km. We present one of their bow shock crossings associated with foreshock ULF waves.

3. Results

On 12 February 2019, four MMS spacecraft crossed Earth's bow shock from the magnetosheath to the solar wind in a string-of-pearls formation with a sequence of MMS2, 1, 4, and 3 (Figures 1.1-1.4). The separation between two adjacent spacecraft is 275, 358, and 229 km, respectively (see the geometry in Figure 2). Upstream of the bow shock, there were fast magnetosonic mode ULF waves with a period of around 20s in the spacecraft frame (Figures 1.1-1.4a and 1.1-1.4b), consistent with commonly observed "30 second waves" (see review by Wilson, 2016). Correlated with the ULF waves, foreshock ions showed periodic inverse energy dispersion (Figure 1d) which will be discussed later. Electron parallel and perpendicular temperatures also oscillated periodically with a phase difference likely due to the ULF wave compression (Figure 1f). Using the mixed mode coplanarity method (Eq. 10.13 in Schwartz, 1998), the calculated bow shock normal observed by MMS2, 1, 4, and 3 was [0.88, -0.35, 0.30], [0.85, -0.46, 0.24], [0.85, -0.27, 0.44], and [0.86, -0.49, 0.11] in GSE, respectively. Such measured results were consistent with [0.88, -0.41, 0.23] in GSE from the Merka et al. (2005) bow shock model. Local θ_{Bn} was around 50° using the average magnetic field. As shock θ_{Bn} was around the boundary between the quasi-parallel and quasi-perpendicular regimes, we simply call it an oblique shock. The angle between the bow shock normal and the spacecraft line was around 20° (Figure 2). Thus, the difference among four spacecraft observations was mainly due to temporal changes. Using conservation of mass flux (Schwartz, 1998), the calculated bow shock normal speed was very small (~10-20 km/s earthward) within the calculation uncertainty.

By comparing the magnetic field data among four spacecraft (Figure 3), we see that the time delay of measured magnetic field structures between two adjacent spacecraft was several seconds. This is because the spacecraft separation was 200-300 km and the magnetic field structures were convecting with the local plasma flow at 100-200 km/s in the magnetosheath and ~330 km/s in the foreshock (Figure 1c) with relative propagation (shown later). However, the time delay between two adjacent spacecraft for the bow shock was ~10-20s, because the bow shock normal speed was very small (the spacecraft motion was several km/s). The four spacecraft thus monitored the bow shock for ~1 min (~7 solar wind ion gyroperiods).

MMS2 first crossed the bow shock (yellow shaded in Figure 3a), which had a gradual transition region (nearly half of the yellow region). Right upstream of the bow shock, a ULF wave (period A, orange shaded in Figure 3a) was interacting with the bow shock, and around one fourth of it had already merged into the bow shock (seen from the filtered magnetic field in Figure S1 in the supporting information). Superposed on ULF wave A, whistler precursor waves (~1 Hz; see Wilson, 2016) were also observed, which can potentially accelerate hot particles (e.g., Wilson et al., 2012), modulate cold particles (e.g., Goncharov et al., 2014), and mix the phase between incident ions and reflected ions (Scholer and Burgess, 2007). Both the ULF wave and whistler precursors were steepening with an enhanced magnetic field (Figures 3a), and their associated electric field increased (Figure 3b), consistent with simulations by Hao et al. (2017) because the increasing magnetic field amplitude produced an induced electric field. Inside wave A, there was a moderate plasma density enhancement (Figure 1.1b), deflection (Figure 1.1c), and heating (Figure 1.1f) with magnitudes between the upstream and downstream values. The steepened waves acted as an extension of the transition region by partially dissipating the incident plasma.

Meanwhile, MMS1, 275 km downstream in the magnetosheath, observed a magnetic structure (yellow in Figure 3c) which looks very similar to the bow shock that MMS2 crossed (yellow in Figure 3a). Based on the time delay, the structure was convecting downstream at ~160 km/s. Upstream of the magnetic structure, MMS1 crossed a new bow shock with a sharper transition region (orange), and the shock normal speed was ~20 km/s earthward from both the time delay from MMS1 to MMS2 and conservation of mass flux. We interpret that as MMS2 crossed the bow shock, the bow shock disturbance continuously generated magnetic perturbations that convected with the magnetosheath plasma flow towards MMS1 (yellow region). As the wavelength of the perturbation was several thousand km, the two spacecraft observed it simultaneously. One period of the perturbation in the magnetosheath acted as a remnant of the bow shock, which contained the information of bow shock disturbance. Similarly, when the bow shock was interacting with the steepened wave A as observed by MMS2 (orange in Figure 3a), another period of the perturbation was being generated in the magnetosheath and convecting towards

MMS1 (orange in Figure 3c). When MMS1 crossed the bow shock, the bow shock had nearly finished interacting with wave A and formed a sharp transition region.

Similarly, MMS4, 358 km further downstream in the magnetosheath, first observed the two remnants of the bow shock that MMS2 and MMS1 crossed (yellow and orange in Figure 3e), respectively. Then MMS4 crossed the new bow shock with a sharp transition region (red) caused by wave B that MMS2 and MMS1 observed. MMS3, 229 km further downstream, observed three remnants of the bow shock crossed by the other three spacecraft. Then MMS3 crossed another new bow shock with a sharp transition region (purple) caused by wave C. Therefore, the four spacecraft observed three reformation cycles and the reformation period was one ULF wave period in the spacecraft frame (~20s).

Next, we analyze the properties of the ULF waves and their corresponding perturbations in the magnetosheath. We band-pass filtered the magnetic field using a frequency range from 0.04 to 0.067 Hz (period from 15 to 25s; see Figure S1) and applied minimum variance analysis (Sonnerup & Scheible, 1998). In the upstream region (above dashed lines in Figure 4), the wave normal direction (top of each panel) had a very strong GSE-X component (intermediate-to-minimum and maximum-to-intermediate eigenvalue ratios are listed on the right of each panel as ratio 1 and ratio 2, respectively). Using the time delay between MMS1 and MMS2 and between MMS4 and MMS3 based on the correlation of filtered B_y of wave E, we calculated that the wave normal speed was sunward (~100 km/s) relative to the ion bulk velocity. Figure 4 shows the wave polarization relative to intrinsically sunward wave normal vectors. As the IMF was sunward (out of the plane in the plasma rest frame or into the plane in the spacecraft frame; also see geometry in Figure 2), they were right-hand polarized in the plasma rest frame and left-hand polarized in the spacecraft frame consistent with previous studies (e.g., Hoppe and Russell, 1983; Eastwood et al., 2002). The same wave period observed by different spacecraft shows similar polarization profile and similar maximum-to-intermediate eigenvalue ratios (Figures 4c and 4g and Figures 4d, 4h, 4l, and 4p), but close to the bow shock the ULF waves became more steepened with larger eigenvalue ratios (Figures 4a, 4f, and 4k). In the magnetosheath (below dashed lines), they were more linearly polarized with larger wave amplitude and also propagating sunward relative to the ion bulk velocity (~50 km/s for wave A). Their normal had less GSE-X component just downstream of the bow shock (Figures 4e and 4o). For other perturbations in the magnetosheath (Figures 4i, 4j, 4m, and 4n), because they were nearly linearly polarized, their normal direction cannot be trusted.

To summarize, upstream of the bow shock, there was a train of "30 second waves" with right-hand polarization and sunward wave normal vectors. As the ULF waves convected anti-sunward in the supersonic solar wind and encountered the bow shock, they changed the upstream conditions periodically because of their large variation in the magnetic field and plasma parameters (Figure 1), which was likely responsible for the periodic reformation of the bow shock. When MMS2 crossed the bow shock, the transition region was gradual (yellow in Figure 3a). ULF wave A was in the middle of interacting with the bow shock. Both the ULF wave and whistler precursors were steepened, which caused the extension of the transition region (orange in Figure 1.1). Such a disturbance at the bow shock generated a nearly linearly polarized compressive perturbation in the magnetosheath as observed by MMS1 (orange in Figure 1.2). When MMS1 crossed the bow shock, the bow shock had nearly finished one reformation cycle with a sharp transition region. It is likely that the sharp (extended) transition region generated the high (low) field strength part of the magnetosheath perturbation. The one-period magnetosheath perturbation acted as the bow shock remnant and convected with the magnetosheath plasma flow (with sunward relative propagation) towards MMS4 and MMS3 (orange in Figures 1.3 and 1.4). Similarly, as waves B and C approached the bow shock, the bow shock completed another two reformation cycles and generated two more bow shock remnants in the magnetosheath. The reformation period was the same as the ULF wave period in the spacecraft frame or the bow shock rest frame (~20s or 2 ion gyroperiods).

This bow shock reformation process due to the upstream ULF waves is different from previous simulations and observations (e.g., Scholer et al., 1993; Lefebvre et al., 2009). In the previous studies, the ULF waves steepened to pulsation-like structures with amplitudes comparable to the shock, eventually becoming the new shock. The reformation cycle was determined from the wave steepening time scale due to interaction with the reflected ions, which was ~10 ion gyroperiods in the simulation by Scholer et al. (1993) and ~35 ion gyroperiods in the observations by Lefebvre et al. (2009). However, our observations show that the reformation cycle was one ULF wave period in the bow shock rest frame (~2 ion gyroperiods). In our observations, only MMS3 observed a pulsation-like structure at wave E (Figure 3g), but it had not participated in bow shock reformation at least during the observation time interval. We thus interpret that the observed reformation was due to the periodic variation of upstream conditions by the ULF waves alone. This result does not mean that steepening to pulsation-like structures cannot result in the reformation of the quasi-parallel bow shock, but only that the ULF waves in the foreshock are sufficient to cause bow shock reformation in and of themselves. Simulations are needed to confirm this process.

Finally, we discuss the response of shock-reflected ions to the bow shock reformation process (Figure 5). There are two shock-reflected ion populations: thermal ions (<1 keV) and suprathermal ions (1-10 keV). In Figure 5c, the suprathermal ions had periodic inverse energy dispersion associated with each wave period. One possibility for the dispersion is that during each reformation cycle, the varying upstream conditions changed θ_{Bn} significantly from 15° to 75° (Figure 5b). As a result, the shock drift acceleration energy or the minimum parallel speed for ions to escape upstream ($\boldsymbol{V_{sw}} \cdot \boldsymbol{\hat{n}} / \cos \theta_{Bn}$; Burgess et al., 2012) changed accordingly. The calculated energy is shown in the ion energy spectrum as the black line in Figure 5c (note the time delay for ions to reach the spacecraft). Although the variation of the bow shock normal is ignored for simplicity, the black line matches the spectra.

To examine the property of reflected thermal ions, we plot the reduced ion velocity distributions along the bow shock normal. Right upstream of the extended transition region, MMS2 observed ions with sunward normal velocity at 50-200 km/s which were the solar wind ions reflected at the bow shock (Figure 5d). Further upstream, reflected ions periodically occur around the beginning of each wave period, because small θ_{Bn} (Figure 5b; also note a few second time delay for ions to reach the spacecraft) favors the reflected ions to escape upstream (e.g., Burgess et al., 2012). The velocity dispersion was likely due to the time-of-flight effect. When MMS1 crossed the bow shock, reflected ions were also observed right and further upstream of the bow shock (Figure 5f). At MMS4, as a new bow shock formed upstream of an old remnant, some reflected ions were trapped between them (Figure 5h), which convected to MMS3 (Figure 5j). As another new bow shock formed at MMS3, some more reflected ions were trapped (Figure 5j). This scenario was similar to simulations by Su et al. (2012a). Some of these trapped ions would eventually merge with magnetosheath ions and contribute to magnetosheath heating, and some of them might experience acceleration and escape upstream.

The significantly varying θ_{Bn} likely plays an important role in the reformation process. When a ULF wave just started to interact with the bow shock, the bow shock became quasi-parallel. This might explain the gradual transition region as observed by MMS2. The quasi-parallel bow shock did not dissipate all the incident ions but reflected some of them forming the foreshock. Later, the bow shock became quasi-perpendicular resulting in a sharp transition region. The reflected ions cannot escape and gyrated back downstream contributing to the dissipation process (e.g., Treumann, 2009). As another ULF wave arrived, the whole cycle repeated. This process complicated how the bow shock and reflected ions interact with the ULF waves.

4. Conclusions

In summary, by using the MMS spacecraft in a string-of-pearls formation, we present the reformation of an oblique bow shock from modulation caused by the "30 second waves" in the ion foreshock. Each time a period of the foreshock ULF waves encountered the bow shock, the bow shock started to reform via an extended transition region. Meanwhile, right downstream in the magnetosheath, a nearly linearly polarized compressive perturbation was generated and convected downstream. After the interaction with one period of the ULF wave, a new bow shock formed with a sharp transition region upstream of the old bow shock remnant. The bow shock experienced three reformation cycles when the four spacecraft crossed it. The reformation mechanism was likely the periodical variation of the upstream conditions caused by the foreshock ULF waves. The reformation process modulated the reflected ions.

Figures

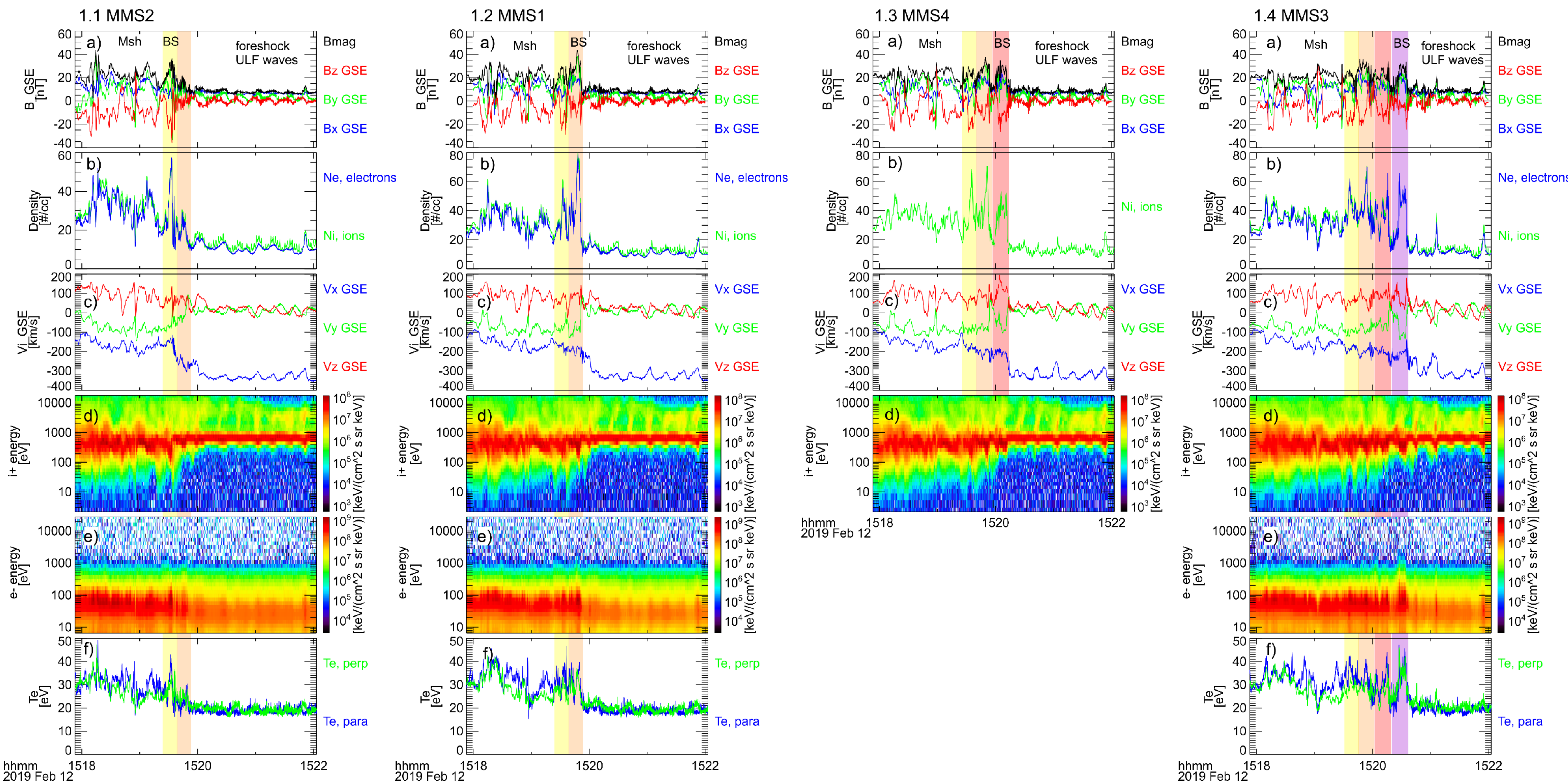
1.1 MMS2
1.2 MMS1
1.3 MMS4
1.4 MMS3
a)
Msh
BS
foreshock
ULF waves
Bmag
Bz GSE
By GSE
Bx GSE
B_GSE [nT]
b)
Density [#/cc]
Ne, electrons
Ni, ions
c)
Vi_GSE [km/s]
Vx GSE
Vy GSE
Vz GSE
d)
i+ energy [eV]
[keV/(cm^2 s sr keV)]
e)
e- energy [eV]
f)
Te [eV]
Te, perp
Te, para
hhmm
2019 Feb 12
1518
1520
1522

Figure 1. Overview of MMS2, 1, 4, and 3 observations (corresponding to Figures 1.1-1.4, respectively). From top to bottom are the magnetic field, density, ion bulk velocity, ion energy flux spectra, electron energy flux spectra, and electron temperature. Note that MMS4 does not have electron data since 2018. Each shaded region with the same color indicates the bow shock and its remnant in the magnetosheath observed by different spacecraft. The darker color is used for the more newly formed bow shock.

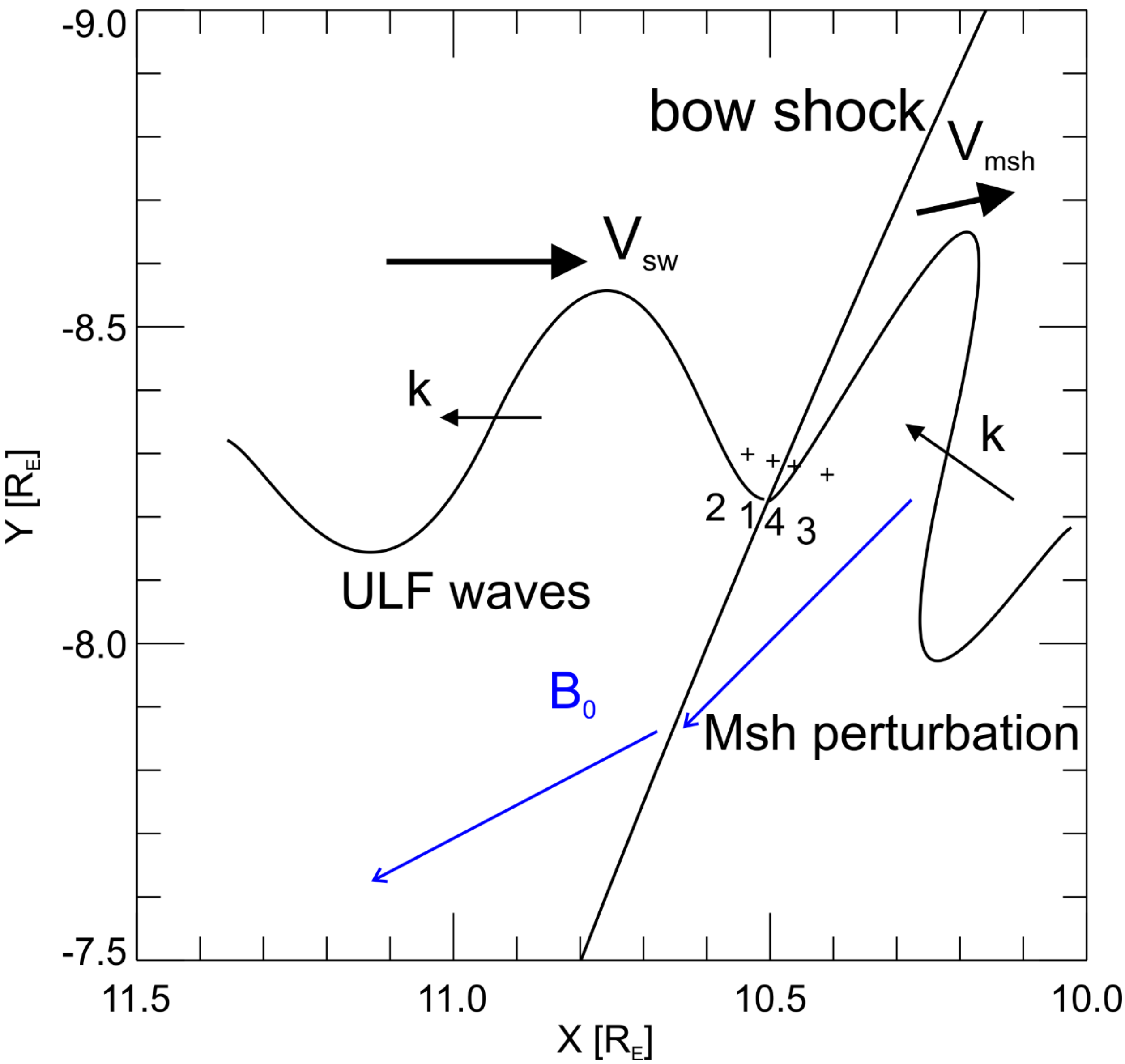

Figure 2. The geometry of the event using Merka et al. (2005) bow shock model (in GSE). The four MMS spacecraft were in a string-of-pearls formation roughly along the bow shock normal. The wavy lines indicate the upstream ULF waves and the magnetosheath perturbations with k vector labeled (from Figure 4). The black arrows indicate the solar wind (sw) and magnetosheath (msh) flow direction.

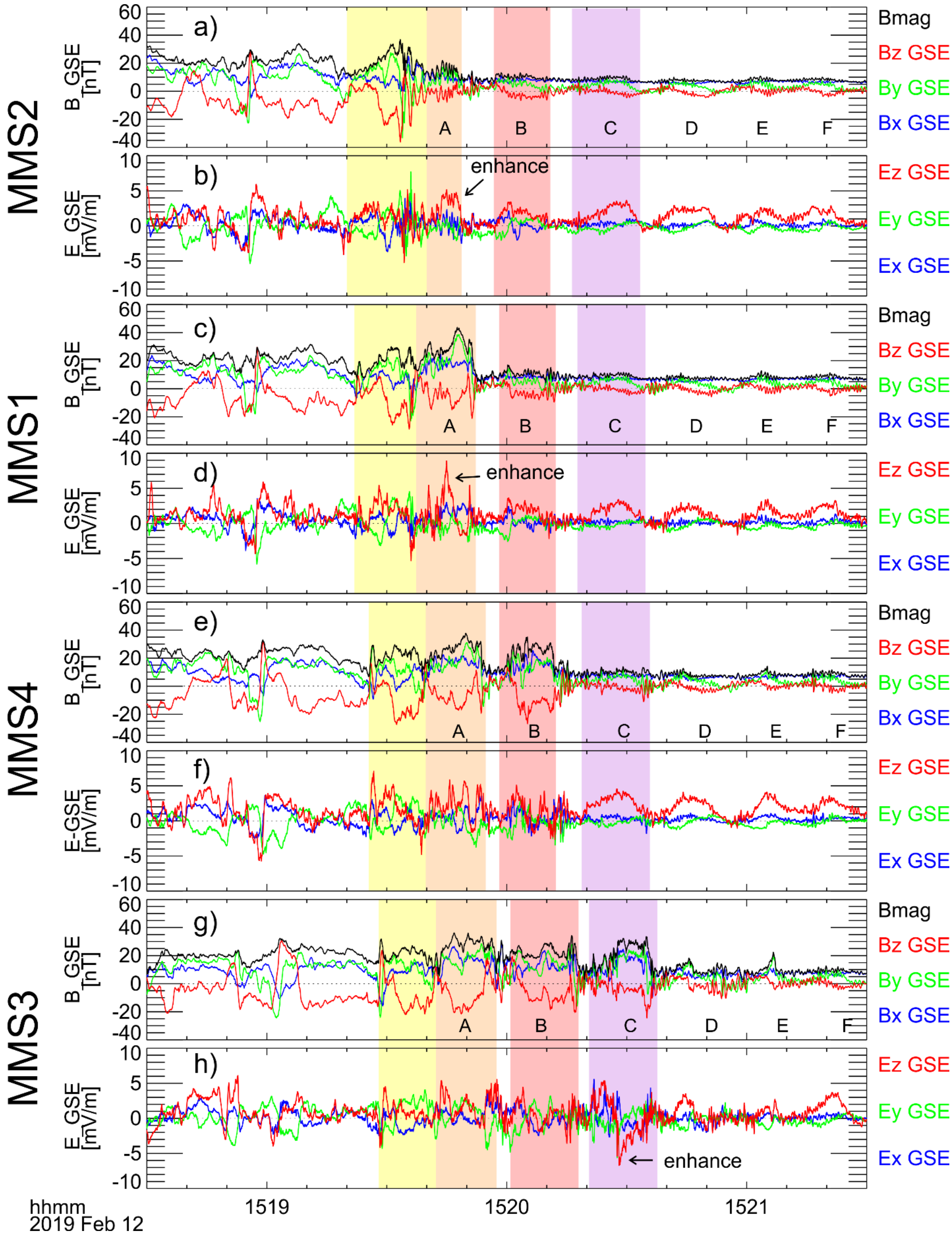
MMS2
MMS1
MMS4
MMS3
a)
b)
c)
d)
e)
f)
g)
h)
B_GSE [nT]
E_GSE [mV/m]
E-GSE [mV/m]
Bmag
Bz GSE
By GSE
Bx GSE
Ez GSE
Ey GSE
Ex GSE
A
B
C
D
E
F
enhance
hhmm
2019 Feb 12
1519
1520
1521

Figure 3. The comparison of the magnetic and electric field among four spacecraft. The color-coded shaded regions (same as Figure 1) indicate the bow shock remnants, the reformed bow shock, and the corresponding upstream ULF waves. The upstream ULF waves are labeled with A-F. Enhanced electric field indicates strong magnetic variation.

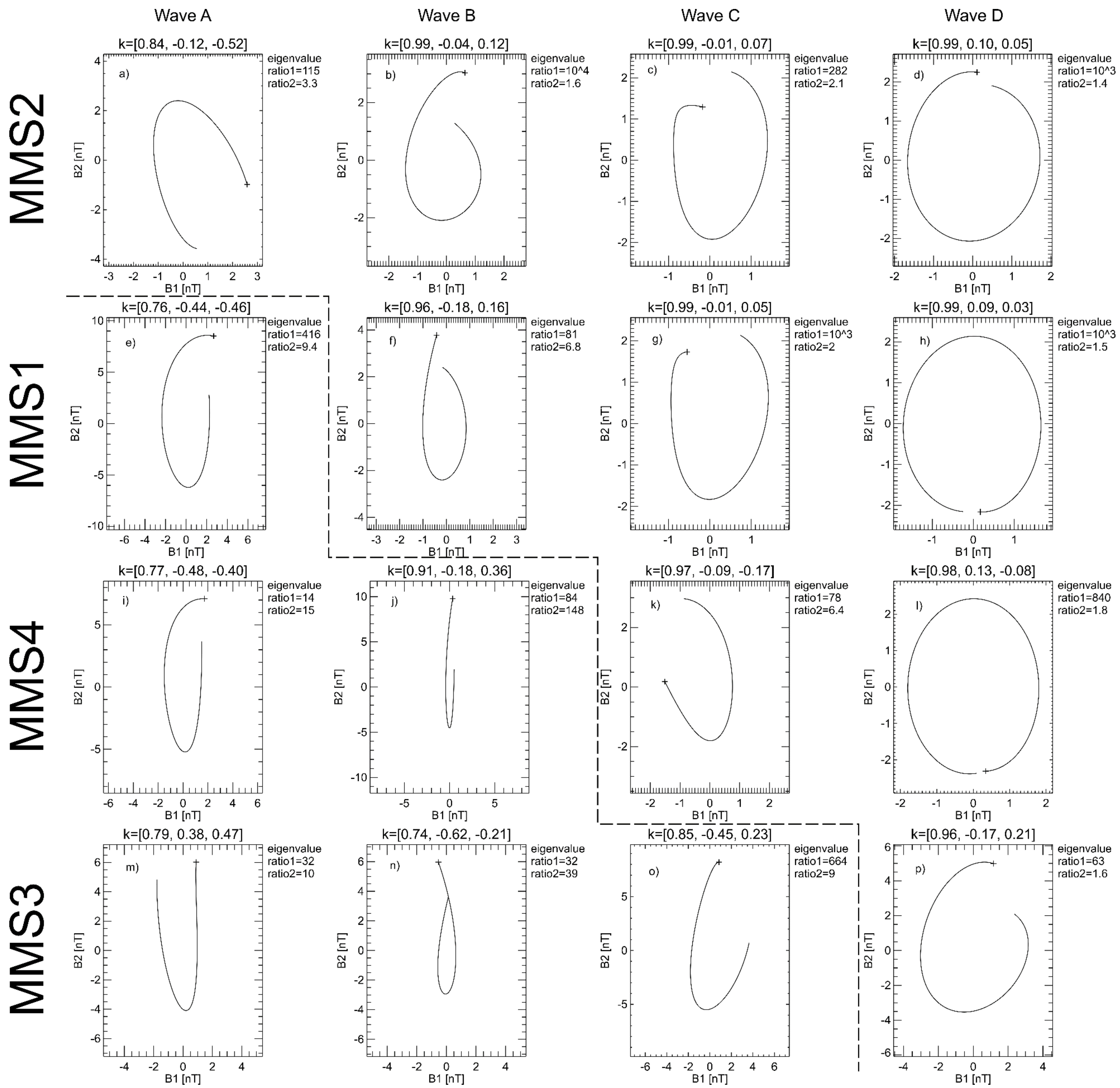

Wave A
Wave B
Wave C
Wave D
MMS2
MMS1
MMS4
MMS3
k=[0.84, -0.12, -0.52]
a)
eigenvalue ratio1=115 ratio2=3.3
k=[0.99, -0.04, 0.12]
b)
eigenvalue ratio1=10^4 ratio2=1.6
k=[0.99, -0.01, 0.07]
c)
eigenvalue ratio1=282 ratio2=2.1
k=[0.99, 0.10, 0.05]
d)
eigenvalue ratio1=10^3 ratio2=1.4
k=[0.76, -0.44, -0.46]
e)
eigenvalue ratio1=416 ratio2=9.4
k=[0.96, -0.18, 0.16]
f)
eigenvalue ratio1=81 ratio2=6.8
k=[0.99, -0.01, 0.05]
g)
eigenvalue ratio1=10^3 ratio2=2
k=[0.99, 0.09, 0.03]
h)
eigenvalue ratio1=10^3 ratio2=1.5
k=[0.77, -0.48, -0.40]
i)
eigenvalue ratio1=14 ratio2=15
k=[0.91, -0.18, 0.36]
j)
eigenvalue ratio1=84 ratio2=148
k=[0.97, -0.09, -0.17]
k)
eigenvalue ratio1=78 ratio2=6.4
k=[0.98, 0.13, -0.08]
l)
eigenvalue ratio1=840 ratio2=1.8
k=[0.79, 0.38, 0.47]
m)
eigenvalue ratio1=32 ratio2=10
k=[0.74, -0.62, -0.21]
n)
eigenvalue ratio1=32 ratio2=39
k=[0.85, -0.45, 0.23]
o)
eigenvalue ratio1=664 ratio2=9
k=[0.96, -0.17, 0.21]
p)
eigenvalue ratio1=63 ratio2=1.6
B1 [nT]
B2 [nT]

Figure 4. The evolution of the magnetic field (start from the cross symbol) within waves A-D and their magnetosheath responses. The horizontal and vertical axes are intermediate and maximum variance direction from MVA, respectively. As the k unit vectors are intrinsically sunward based on the spacecraft timing listed on top of each panel, IMF points out of the plane in the plasma rest frame or into the plane in the spacecraft frame. The intermediate-to-minimum and maximum-to-intermediate eigenvalue ratios (ratio1 and ratio2) are listed on the right of each panel. The upstream and downstream regions are separated by dashed lines. The magnetic field in the solar wind points out of the plane, whereas in the magnetosheath the k vector was nearly perpendicular to the background magnetic field.

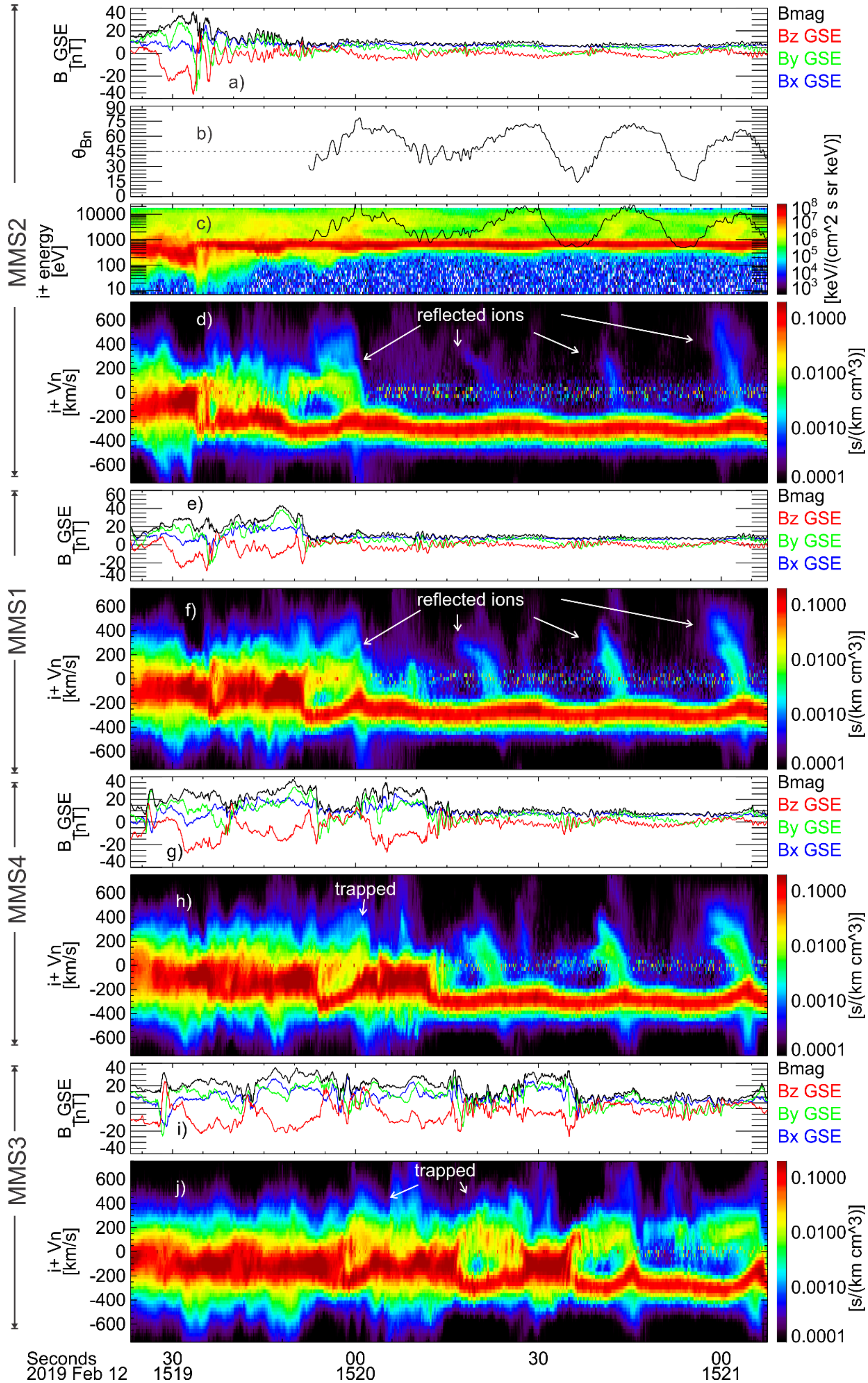

Bmag
Bz GSE
By GSE
Bx GSE
B_GSE [nT]
a)
θ_{Bn}
b)
MMS2
i+ energy [eV]
c)
[keV/(cm^2 s sr keV)]
d)
reflected ions
i+ Vn [km/s]
[s/(km cm^3)]
e)
MMS1
f)
MMS4
g)
h)
trapped
MMS3
i)
j)
Seconds
2019 Feb 12
30
1519
00
1520
30
00
1521

Figure 5. MMS observations of reflected ions. From top to bottom are: (a)-(d) MMS2 observations of the magnetic field, θ_{Bn}, ion energy spectrum (the black line is calculated from the shock drift acceleration model), and the reduced ion velocity distributions along the bow shock normal direction V_n; (e)-(j) MMS1, 4 and 3 observations of the magnetic field and reduced ion V_n distribution, respectively.

Acknowledgement

We acknowledge the International Space Science Institute (ISSI) for providing a collaborative opportunity for this work. T. Z. L. is supported by the NASA Living With a Star Jack Eddy Postdoctoral Fellowship Program, administered by the Cooperative Programs for the Advancement of Earth System Science (CPAESS). H. Z. is partially supported by NSF AGS-1352669. MMS data are available at MMS Science Data Center (https://lasp.colorado.edu/mms/sdc/public/). We thank the SPEDAS software team and NASA's Coordinated Data Analysis Web (CDAWeb, http://cdaweb.gsfc.nasa.gov/) for their analysis tools and data access. The SPEDAS software (see Angelopoulos et al. (2019)) is available at http://themis.ssl.berkeley.edu.

References

Angelopoulos, V., Cruce, P., Drozdov, A. et al. Space Sci Rev (2019) 215: 9. https://doi.org/10.1007/s11214-018-0576-4

Archer, M.O., T.S. Horbury, J.P. Eastwood, J.M. Weygand, T.K. Yeoman, Magnetospheric response to magnetosheath pressure pulses: a low-pass filter effect. J. Geophys. Res. 118, 5454–5466 (2013). https://doi.org/10.1002/jgra.50519.

Burch, J. L., Moore, T. E., Torbert, R. B., & Giles, B. L. (2016). Magnetospheric multiscale overview and science objectives. Space Science Reviews, 199(1 - 4), 5 – 21. https://doi.org/10.1007/s11214-015-0164-9

Burgess, D. (1989), Cyclic behavior at quasi-parallel collisionless shocks, Geophys. Res. Lett., 16(5), 345–348, doi:10.1029/GL016i005p00345.

Burgess, D., Möbius, E. & Scholer, M. (2012). Ion Acceleration at the Earth's Bow Shock. Space Sci Rev 173, 5–47. https://doi.org/10.1007/s11214-012-9901-5

Dimmock, A. P., et al. (2019), Direct evidence of nonstationary collisionless shocks in space plasmas, Science Advances, 5, doi:10.1126/sciadv.aau9926.

Eastwood, J. P., Balogh, A., Dunlop, M. W., Horbury, T. S., and Dandouras, I., Cluster observations of fast magnetosonic waves in the terrestrial foreshock, Geophys. Res. Lett., 29 (22), 2046, doi:10.1029/2002GL015582, 2002.

Eastwood, J.P., Lucek, E.A., Mazelle, C. et al. (2005). The Foreshock. Space Sci Rev 118, 41–94. https://doi.org/10.1007/s11214-005-3824-3

Ergun, R. E., Tucker, S., Westfall, J., Goodrich, K. A., Malaspina, D. M., Summers, D.,…Cully, C. M. (2016). The axial double probe and fields signal processing for the MMS mission. Space Science Reviews, 199, 167–188.

Fairfield, D. H. (1969), Bow shock associated waves observed in the far upstream interplanetary medium, J. Geophys. Res., 74 (14), 3541– 3553, doi:10.1029/JA074i014p03541.

Fairfield, D. H. (1974), Whistler waves observed upstream from collisionless shocks, J. Geophys. Res., 79 (10), 1368– 1378, doi:10.1029/JA079i010p01368.

Fairfield, D. H., and Feldman, W. C. (1975), Standing waves at low Mach number laminar bow shocks, J. Geophys. Res., 80 (4), 515– 522, doi:10.1029/JA080i004p00515.

Gingell, I., Schwartz, S. J., Burgess, D., Johlander, A., Russell, C. T., Burch, J. L., …Wilder, F. (2017). MMS observations and hybrid simulations of surface ripples at a marginally quasi-parallel shock. Journal of Geophysical Research: Space Physics, 122, 11,003–11,017. https://doi.org/10.1002/2017JA024538

Goncharov, O., J. Šafránková, Z. Nˇemeˇcek, L. Pˇrech, A. Pitˇna, and G. N. Zastenker (2014), Upstream and downstream wave packets associated with low-Mach number interplanetary shocks, Geophys. Res. Lett., 41, 8100–8106

Hao, Y., Q. Lu, X. Gao, and S. Wang (2016), Ion dynamics at a rippled quasi-parallel shock: 2D hybrid simulations, Astrophys. J., 823, 7.

Hao, Y., X. Gao, Q. Lu, C. Huang, R. Wang, and S. Wang (2017), Reformation of rippled quasi-parallel shocks: 2-D hybrid simulations, J. Geophys. Res. Space Physics, 122, 6385–6396, doi:10.1002/2017JA024234.

Hietala, H., Laitinen, T. V., Andréeová, K., Vainio, R., Vaivads, A., Palmroth, M., et al. (2009). Supermagnetosonic jets behind a collisionless quasiparallel shock. Physical Review Letters, 103(24), 001. https://doi.org/10.1103/PhysRevLett.103.245001

Hietala, H., Partamies, N., Laitinen, T. V., Clausen, L. B. N., Facskó, G., Vaivads, A., et al. (2012). Supermagnetosonic subsolar magnetosheath jets and their effects: From the solar wind to the ionospheric convection. Annals of Geophysics, 30(1), 33–48. https://doi.org/10.5194/angeo-3033-2012

Hietala, H., & Plaschke, F. (2013). On the generation of magnetosheath high-speed jets by bow shock ripples. Journal of Geophysical Research: Space Physics, 118, 7237–7245. https://doi.org/10.1002/2013JA019172

Hoppe, M. M., and Russell, C. T. (1983), Plasma rest frame frequencies and polarizations of the low-frequency upstream waves: ISEE 1 and 2 Observations, J. Geophys. Res., 88 (A3), 2021–2027, doi:10.1029/JA088iA03p02021.

Johlander, A. et al. (2016), Rippled Quasiperpendicular Shock Observed by the Magnetospheric Multiscale Spacecraft, Phys. Rev. Lett. 117, 16, doi:10.1103/PhysRevLett.117.165101

Lefebvre, B., Seki, Y., Schwartz, S. J., Mazelle, C., and Lucek, E. A. (2009), Reformation of an oblique shock observed by Cluster, J. Geophys. Res., 114, A11107, doi:10.1029/2009JA014268.

Lembege, B. and Savoini, P. (1992). Nonstationarity of a two-dimensional quasiperpendicular supercritical collisionless shock by self-reformation. Physics of Fluids B: Plasma Physics 4, 3533. https://doi.org/10.1063/1.860361

Lin, Y., and Wang, X. (2005), Three-dimensional global hybrid simulation of dayside dynamics associated with the quasi - parallel bow shock, J. Geophys. Res., 110, A12216, doi:10.1029/2005JA011243.

Lindqvist, P.-A., Olsson, G., Torbert, R. B., King, B., Granoff, M., Rau, D., et al. (2016). The spin-plane double probe electric field instrument for MMS. Space Science Reviews, 199(1-4), 137–165. https://doi.org/10.1007/s11214-014-0116-9

Liu, Z., Turner, D. L., Angelopoulos, V., & Omidi, N. (2015). THEMIS observations of tangential discontinuity-driven foreshock bubbles. Geophysical Research Letters, 42, 7860–7866. https://doi.org/10.1002/2015GL065842

Liu, T. Z., Hietala, H., Angelopoulos, V., & Turner, D. L. (2016). Observations of a new foreshock region upstream of a foreshock bubble's shock. Geophysical Research Letters, 43, 4708–4715. https://doi.org/10.1002/2016GL068984

Liu, T. Z., Lu, S., Angelopoulos, V., Lin, Y., & Wang, X. Y. (2018). Ion acceleration inside foreshock transients. Journal of Geophysical Research: Space Physics, 123, 163–178. https://doi.org/10.1002/2017JA024838

Liu, T. Z., Hietala, H., Angelopoulos, V., Omelchenko, Y., Roytershteyn, V., & Vainio, R. (2019). THEMIS observations of particle acceleration by a magnetosheath jet - driven bow wave. Geophysical Research Letters, 46. https://doi.org/10.1029/2019GL082614

Liu, T. Z., Hietala, H., Angelopoulos, V., Vainio, R., & Omelchenko, Y. (2020a). Electron acceleration by magnetosheath jet-driven bow waves. Journal of Geophysical Research: Space Physics, 125, e2019JA027709. https://doi.org/10.1029/2019JA027709

Liu, T. Z., Hietala, H., Angelopoulos, V., Omelchenko, Y., Vainio, R., & Plaschke, F. (2020b). Statistical study of magnetosheath jet-driven bow waves. Journal of Geophysical Research: Space Physics, 125, e2019JA027710. https://doi.org/10.1029/2019JA027710

Lobzin, V. V., Krasnoselskikh, V. V., Bosqued, J.-M., Pinçon, J.-L., Schwartz, S. J., and Dunlop, M. (2007), Nonstationarity and reformation of high-Mach-number quasiperpendicular shocks: Cluster observations, Geophys. Res. Lett., 34, L05107, doi:10.1029/2006GL029095.

Madanian, H., Schwartz, S. J., Halekas, J. S., & Wilson, L. B. (2020). Nonstationary quasiperpendicular shock and ion reflection at Mars. Geophysical Research Letters, 47, e2020GL088309. https://doi.org/10.1029/2020GL088309

Matsukiyo S. and Scholer M. (2006), On reformation of quasi-perpendicular collisionless shocks, AdSpR 38 57

Merka, J., Szabo, A., Slavin, J. A., and Peredo, M. (2005), Three-dimensional position and shape of the bow shock and their variation with upstream Mach numbers and interplanetary magnetic field orientation, J. Geophys. Res., 110, A04202, doi:10.1029/2004JA010944.

Omidi, N., J. P. Eastwood, and D. G. Sibeck (2010), Foreshock bubbles and their global magnetospheric impacts, J. Geophys. Res., 115, A06204, doi:10.1029/2009JA014828.

Omidi, N., Lee, S. H., Sibeck, D. G., Turner, D. L., Liu, T. Z., & Angelopoulos, V. (2020). Formation and topology of foreshock bubbles. Journal of Geophysical Research: Space Physics, 125, e2020JA028058. https://doi.org/10.1029/2020JA028058

Pollock, C., Moore, T., Jacques, A., Burch, J., Gliese, U., Saito, Y., et al. (2016). Fast plasma investigation for magnetospheric multiscale. Space Science Reviews, 199(1 - 4), 331 – 406. https://doi.org/10.1007/s11214-016-0245-4

Russell, C. (2007), Upstream whistler-mode waves at planetary bow shocks: A brief review. J. Atmos. Solar-Terr. Phys., 69, 1739–1746, doi:10.1016/j.jastp.2006.11.004.

Russell, C. T., Anderson, B. J., Baumjohann, W., Bromund, K. R., Dearborn, D., Fischer, D., et al. (2016). The magnetospheric multiscale magnetometers. Space Science Reviews, 199(1-4), 189–256. https://doi.org/10.1007/s11214-014-0057-3

Scholer, M., and Burgess, D. (1992), The role of upstream waves in supercritical quasi-parallel shock re-formation, J. Geophys. Res., 97 (A6), 8319– 8326, doi:10.1029/92JA00312.

Scholer, M. (1993), Upstream waves, shocklets, short large-amplitude magnetic structures and the cyclic behavior of oblique quasi-parallel collisionless shocks, J. Geophys. Res., 98, 47–57, doi:10.1029/92JA01875.

Scholer, M., M. Fujimoto, and H. Kucharek (1993), 2-dimensional simulations of supercritical quasi-parallel shocks—Upstream waves, downstream waves and shock re-formation, J. Geophys. Res., 98, 18,971–18,984, doi:10.1029/93JA01647

Scholer, M., and Burgess, D. (2007). Whistler waves, core ion heating, and nonstationarity in oblique collisionless shocks, Physics of Plasmas 14, 072103. https://doi.org/10.1063/1.2748391

Schwartz, S. J., Burgess, D., Wilkinson, W. P., Kessel, R. L., Dunlop, M., and Lühr, H. (1992), Observations of short large-amplitude magnetic structures at a quasi-parallel shock, J. Geophys. Res., 97 (A4), 4209– 4227, doi:10.1029/91JA02581.

Schwartz, S. J. (1998), Shock and discontinuity normal, Mach numbers, and related parameters, from Analysis Methods for Multi-Spacecraft Data, edited by G. Paschmann and P. W. Daly, pp. 249–270.

Sonnerup, B. U. Ö., & Scheible, M. (1998). Minimum and maximum variance analysis. In G. Paschmann & P. W. Daly (Eds.), Analysis methods for multi spacecraft data (pp. 185–215). Bern, Switzerland: European Space Agency.

Su, Y., Q. Lu, C. Huang, M. Wu, X. Gao, and S. Wang (2012a), Particle acceleration and generation of diffuse superthermal ions at a quasi-parallel collisionless shock: Hybrid simulations, J. Geophys. Res., 117, A08107, doi:10.1029/2012JA017736.

Su, Y., Q. Lu, X. Gao, C. Huang, and S. Wang (2012b), Ion dynamics at supercritical quasi-parallel shocks: Hybrid simulations, Phys. Plasmas, 19, 092108.

Thomas, V. A., D. Winske, and N. Omidi (1990), Reforming super-critical quasi-parallel shocks, 1. One- and two-dimensional simulations, J. Geophys. Res., 95, 18,809–18,819, doi:10.1029/JA095iA11p18809.

Treumann, R. A. (2009), Fundamentals of collisionless shocks for astrophysical application, 1. Non-relativistic shocks. Astron. Astrophys. Rev. 17, 409.

Turner D. L., N. Omidi, D. G. Sibeck, and V. Angelopoulos (2013), First observations of foreshock bubbles upstream of Earth's bow shock: Characteristics and comparisons to HFAs, J. Geophys. Res., VOL. 118, 1552–1570, doi:10.1002/jgra.50198.

Turner, D. L., Liu, T. Z., Wilson, L. B., Cohen, I. J., Gershman, D. G., Fennell, J. F., et al. (2020). Microscopic, multipoint characterization of foreshock bubbles with Magnetospheric Multiscale (MMS). Journal of Geophysical Research: Space Physics, 125, e2019JA027707. https://doi.org/10.1029/2019JA027707

Umeda, T., Yamao, M., & Yamazaki, R. (2009). Electron acceleration at a low Mach number perpendicular collisionless shock. *Astrophysical Journal*, *695*, 574 – 579. https://doi.org/10.1088/0004-637X/695/1/574

Wang, B., Nishimura, Y., Hietala, H., Lyons, L., Angelopoulos, V., Plaschke, F., et al. (2018). Impacts of magnetosheath high-speed jets on the magnetosphere and ionosphere measured by optical imaging and satellite observations. Journal of Geophysical Research: Space Physics, 123, 4879–4894. https://doi.org/10.1029/2017JA024954.

Wilson, L. B., III, et al. (2012), Observations of electromagnetic whistler precursors at supercritical interplanetary shocks, Geophys. Res. Lett., 39, L08109

Wilson, L.B., III (2016). Low Frequency Waves at and Upstream of Collisionless Shocks. In Low‐Frequency Waves in Space Plasmas (eds A. Keiling, D.‐H. Lee and V. Nakariakov). doi:10.1002/9781119055006.ch16

Winske, D., N. Omidi, K. B. Quest, and V. A. Thomas (1990), Re-forming supercritical quasi-parallel shocks: 2. Mechanism for wave generation and front re-formation, J. Geophys. Res., 95(A11), 18,821–18,832, doi:10.1029/JA095iA11p18821.

Yang, Z., Y. D. Liu, A. Johlander, G. K. Parks, B. Lavraud, E. Lee, W. Baumjohann, R. Wang, and J. L. Burch (2020), MMS direct observations of kinetic-scale shock self-reformation, ApJL, 901, 1, https://doi.org/10.3847/2041-8213/abb3ff